Investigation of manufacturing techniques to develop controlled flaws for x-ray computed tomography reliability assessment

F. Kim, S. Robinson, N. Klimov, J. H. Scott

F. H. Kim, S. M. Robinson, N. N. Klimov, J. H. J. Scott, "Investigation of manufacturing techniques to develop controlled flaws for x-ray computed tomography reliability assessment ," Proc. SPIE 12491, 8th International Workshop on Reliability of NDT/NDE, 1249108 (25 April 2023); doi: 10.1117/12.2660458

SPIE.

Event: SPIE Smart Structures + Nondestructive Evaluation, 2023, Long Beach, California, United States

Investigation of manufacturing techniques to develop controlled flaws for X-ray computed tomography reliability assessment

F.H. Kim*[a], S.M. Robinson[a], N.N. Klimov[a], and J.H.J. Scott[a]
[a]National Institute of Standards and Technology, 100 Bureau Drive, Gaithersburg, MD, USA 20899†

ABSTRACT

Various micro and nano-manufacturing techniques were investigated to create controlled flaws for X-ray computed tomography (XCT) phantoms. We explored the use of focused ion beam, laser micromachining, and projection photolithography with deep reactive ion etching to generate controlled pores from 100s of micrometers to a few micrometers in size. Principles of each technique, fabrication results, and the calibration processes for the manufactured pores are discussed, as well as possible assembly techniques for building up larger pore-containing structure and initial results for such assemblies. Example scanning electron microscope and XCT measurements of the phantoms are shown.

Keywords: X-ray computed tomography, reliability, probability of detection, visibility, phantom, segmentation, seeded defects, additive manufacturing

1. INTRODUCTION

X-ray computed tomography (XCT) is a non-destructive testing (NDT) method for inspection of advanced manufactured components including those made through additive manufacturing (AM). NDT reliability assessment is an important aspect of part qualification workflow, and the probability of detection (POD) provides quantitative information to qualify the NDT examination process. POD can be evaluated based on practical inspection trials of realistic flaw specimens (i.e., phantoms). Only a handful of test phantoms have been developed for XCT measurements with the purpose of directly or indirectly measuring spatial resolution [1-3]. These measurements provide theoretical estimates of spatial resolution of an ideal object for visual detection. However, they are not designed to estimate POD and do not perform well on actual part geometry. Although XCT images are often examined by a human inspector, utilization of automated/assisted flaw detection algorithms (or human/machine interaction) to detect flaws is growing, and these approaches require different types of phantoms that incorporate representative flaws. Some challenges associated with developing such phantoms for XCT measurements remain. We investigated various manufacturing techniques to develop controlled flaws and discuss the initial results of these investigations.

1.1 Previous approaches

An XCT signal response POD method was demonstrated using a phantom developed through a laser powder bed fusion (LPBF) AM process [4]. Six different sizes of cubes were designed, and the voids were filled with metal powders. Higher-resolution XCT scans were used as reference measurements for the encapsulated features. In a follow-up study [5], AM was combined with a traditional manufacturing process (electro discharge machining) to create surface features. The features were calibrated using a focus variation microscope, and a mating piece was used to encapsulate the feature for XCT measurements. Merging with XCT simulation was also demonstrated to complement limited and costly experimental measurements. When using the AM method, however, it is difficult to control the pore size, and the resulting AM parts are also prone to having unintentional flaws (e.g., gas pores or near-surface pores), which can complicate false call analysis. Alternative approaches were investigated in this research.

* felix.kim@nist.gov

8th International Workshop on Reliability of NDT/NDE, edited by Daniel Kanzler, Norbert G. Meyendorf, Proc. of SPIE Vol. 12491, 1249108 · © 2023 SPIE
0277-786X · doi: 10.1117/12.2660458

2. MANUFACTURING TECHNIQUES

2.1 Focused Ion Beam

Focused ion beam (FIB) is a mechanical machining technique in which the drill bit is replaced with a small diameter ion beam [6]. A liquid metal ion source (e.g., utilizing Ga^+ ions) is typically used, but a plasma source (e.g., Xe) is also available for plasma FIB. The main advantage of the plasma FIB is the faster material removal rate (≈ 50x) compared to Ga-FIB with a larger ion beam spot size. FIB is often used to reveal hidden cross sections for microstructural analysis or for extracting a smaller sample for a subsequent analysis using a different characterization methodology (e.g., atom probe tomography or transmission electron microscopy). In this work we explored the advantages of the technique as a method to generate artificial flaws.

2.2 Laser micromachining

Laser micromachining uses laser ablation, which is the process of removing matter from a solid by an energy-induced transient disequilibrium in the lattice [6]. The removal of material depends on material-specific absorbance of laser wavelength, laser pulse width, and laser characteristics (e.g., beam energy profile, energy density, and the wavelength). A laser beam with an ultrashort pulse width can transmit energy into the material at high power, transforming some of the target material into plasma state. In this case, the material goes from a solid phase to a volatile gas + plasma phase bypassing the molten phase. For materials that are hard to drill with mechanical tools, laser micromachining can be a feasible option.

2.3 Lithography and etching

Projection photolithography with deep reactive ion etching (DRIE) is a manufacturing technique used frequently in the manufacture of semiconductor devices. Lithography is a technique of transferring a pattern onto a solid material such as a silicon wafer. Photolithography is the most widely used form of lithography, which typically uses a light source and a photomask to transfer a pattern to the photoresist deposited on the surface of a wafer. DRIE is a dry etching technique to remove material based on the transferred pattern. DRIE results in anisotropic etching compared to wet etching techniques and exhibits high accuracy, repeatability, and throughput. The process, however, is optimized for selected materials (e.g., Si, GaAs, Ge) and planar geometries with defined sizes (e.g., wafers).

3. ASSEMBLY METHODS

3.1 Insertable design

Li et al. [7] presented the concept of inserts for an AM part geometry for XCT image quality analysis. By exploiting this insert concept and combining it with the mating concept [5], inserts with designed features are being developed. An example is shown in Figure 1, where pores will be created on one of the pins and the other pin will be used as a mating piece. Example pins with manufactured pores will be shown in section 4. Our goal is to demonstrate the capability to develop such inserts using FIB, laser micromachining, and other relevant manufacturing techniques.

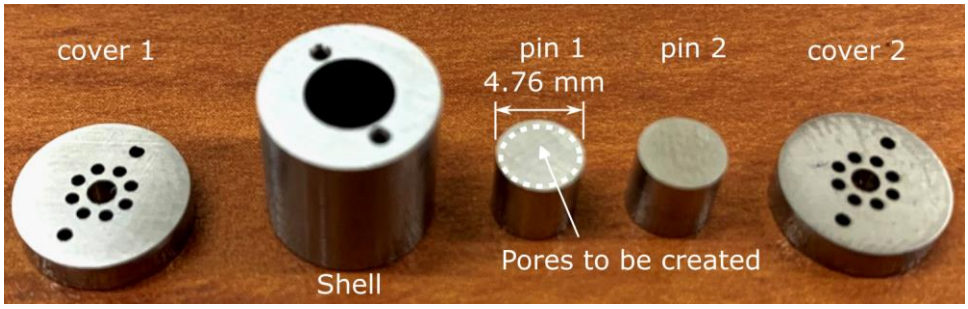

Figure 1: Example phantom design with insertable pins.

3.2 Stacking and bonding

For the Si chips developed through lithography and the DRIE process, the chip stacking approach is explored. The use of adhesives, direct (fusion) bonding, or a combination are also being explored. The use of adhesive would be an easier approach for bonding chips, but the adhesive can be seen in XCT images, which may complicate some volumetric

analyses. Direct bonding, on the other hand, is more difficult to achieve, but the interface between the chips is fully fused once successful. Direct bonding is extremely sensitive to the cleanliness of the chip/wafer surface, and a chemical cleaning process is often needed to achieve the required hydrophilic or hydrophobic surfaces.

4. RESULTS AND DISCUSSION

4.1 Focused Ion Beam

An FEI Nova NanoLab 600 FIB/scanning electron microscopy (SEM) system[‡] with a Ga ion source was used for the initial demonstration. On a commercially available wrought stainless steel piece (17-4 precipitation hardening (PH)), varying diameters and depths of nominally cylindrical blind holes were generated using FIB. An application file sets the beam dwell time, beam diameter overlaps, and volume of material removed per dose, and it dictates the material removal rate. Based on these parameters, the total mill time can be estimated to achieve the desired defect volume. We used the Si FIB application file for the feasibility test, and it showed acceptable manufacturing results for the 17-4 stainless steel material. Optimizing the application file for the 17-4 stainless steel material is possible, but it was out of scope of this paper. For a POD study, which is the main application of the phantom, it is acceptable to have minor deviation from designed dimensions provided the actual size can be measured. A collection of cylindrical holes was created up to 40 µm diameter × 40 µm deep in this system, which took about 8 h of ion beam milling time. Example holes (designed size of 10 µm × 10 µm, 20 µm × 20 µm, and 40 µm × 40 µm) are shown in Figure 2. Actual hole dimensions can be further measured from the images. The hole of 50 µm × 50 µm required over 20 h. The system used was not stable over that time so manufacturing was not successful. This can be improved by using a different or a newer system, which would likely reduce the FIB time. Plasma-FIB is also expected to improve the throughput if the cost is not prohibitive for the process. For our application, we found FIB to be useful for generating cylindrical features below 50 µm diameter × 50 µm deep with reasonable manufacturing time and cost.

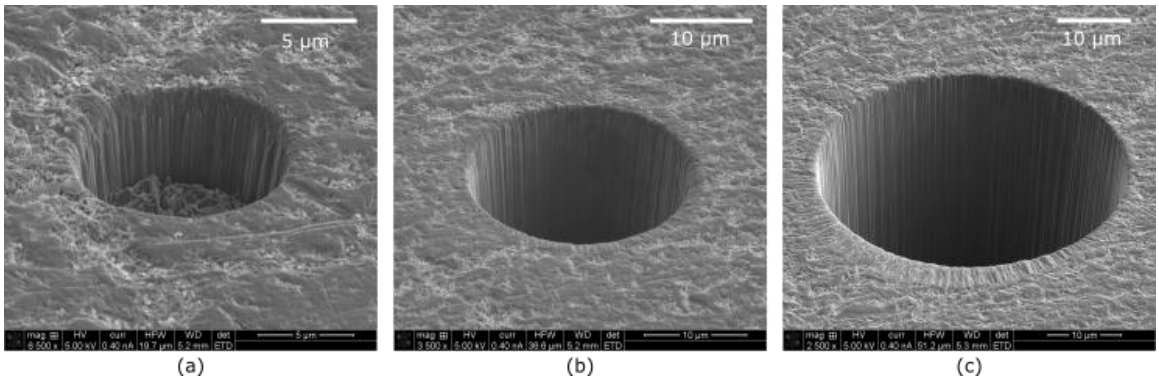

Figure 2: (a) 10 µm × 10 µm hole, (b) 20 µm × 20 µm hole, and (c) 40 µm × 40 µm holes generated with FIB.

4.2 Laser micromachining

Different sizes (200 µm to 25 µm in diameter) and depths (100 µm to 50 µm in depth) of blind holes were generated on a polished stainless steel substrate (17-4 PH) using a laser micromachining service vendor. The pattern on a pin is shown in Figure 3a and a stereoscope image of the manufactured hole pattern is shown in Figure 3b. Example SEM images are shown Figure 4. Figure 4a and Figure 4b show nominally designed 200 µm hole with 100 µm and 50 µm depths. While the hole diameters at the top surface are close to target dimensions, significant amounts of tapering occurred on the side surfaces toward the bottom of the holes. The material was removed in several passes, and tapering was necessary to avoid redeposition of the ablated materials in the center of the hole. A relatively flat bottom surface was achieved with microscopic holes as shown in Figure 4c. A tapered side with some ridges, possibly due to rapid cooling, is shown in

[‡] FEI is currently a subsidiary of Thermo Fisher Scientific. Certain equipment, instruments, software, or materials, commercial or non-commercial, are identified in this paper in order to specify the experimental procedure adequately. Such identification is not intended to imply recommendation or endorsement of any product or service by NIST, nor is it intended to imply that the materials or equipment identified are necessarily the best available for the purpose.

Figure 4d. The smaller holes shown in Figure 4e and Figure 4f were also not created properly. Blind holes in this size range can be created using FIB.

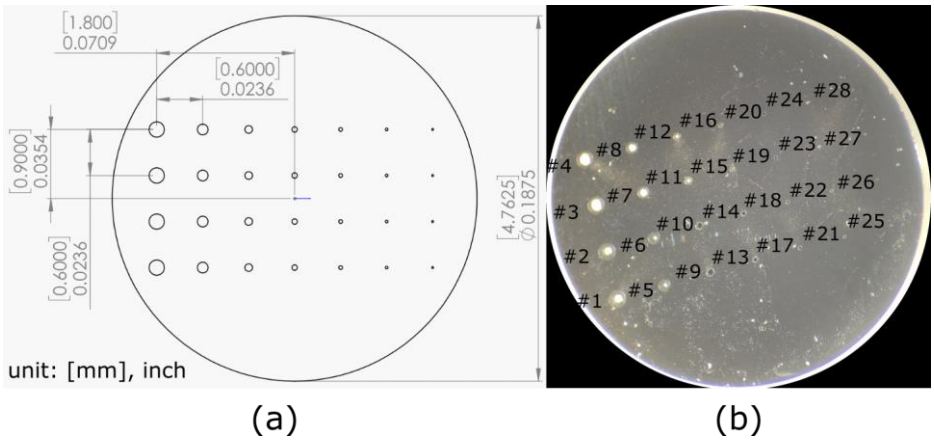

Figure 3: (a) Hole pattern for laser micromachining and (b) Stereoscope image of the created blind holes.

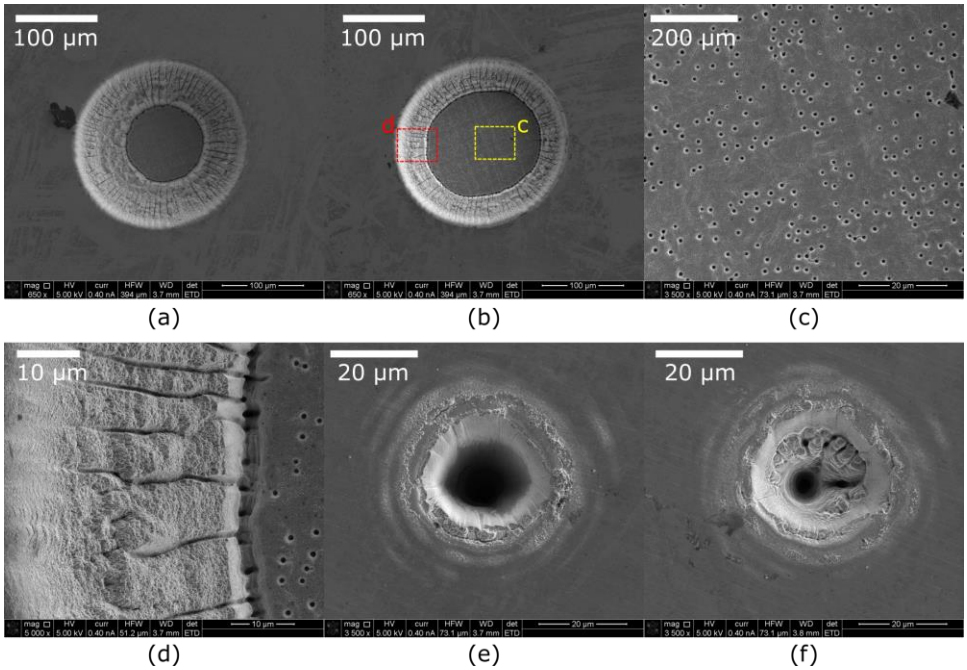

Figure 4: SEM images of (a) hole #1 (200 µm × 100 µm), (b) hole #3 (200 µm × 50 µm), (c) hole #3 bottom surface, (d) hole #3 side wall, (e) hole #17 (50 µm × 100 µm), and (f) hole #19 (50 µm × 50 µm).

In addition to creating the blind holes, through holes were also generated on thin foils of stainless steel material. A 50 µm diameter hole was generated on a 50 µm-thick foil, and a 100 µm hole was generated on a 100 µm-thick foil. Figure 5a and Figure 5b show the laser beam exit surface of the thin foil, and Figure 5c and Figure 5d show the laser beam entrant surface of the thin foil. Tapering is still observed at the laser beam entrant surface, but the SEM images in Figure 5d show a higher quality surface finish with reduced tapering angle compared to those on blind holes. The actual manufacturing time using pico to femto-second laser ablation processes is much shorter than FIB.

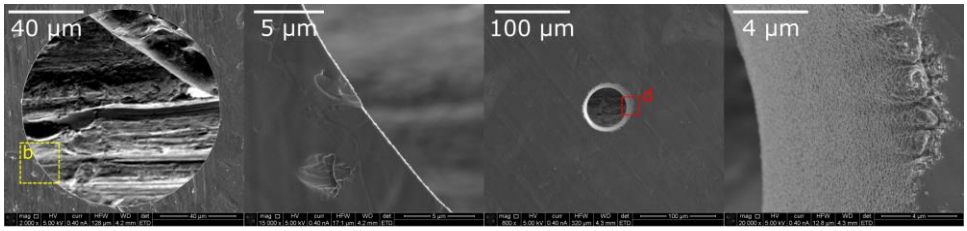

Figure 5: (a) Laser beam exit surface of 100 µm hole, (b) magnified region of surface in (a), (c) laser beam entrant surface of 50 µm hole, and (d) magnified region of surface in (c).

4.3 Lithography with DRIE

Stepper photolithography was used to create repeated copies of the pattern of interest across a 100 mm wafer. A dark field photomask (the created features, such as holes, are transparent to light) will polymerize a positive photoresist in those areas. After the polymerized photoresist is washed away, the exposed Si wafer was etched using DRIE. DRIE uses a combination of chemical and mechanical etching through the Bosch process, where several loops of passivation and etching steps were used to generate anisotropic holes. Each design was repeated in a 2 × 2 pattern on a 9.875 mm × 9.875 mm chip area. Several chips were created on a wafer and the chips were diced accordingly.

Direct bonding between a patterned chip and a blank chip was implemented afterwards. The chips are fused without any adhesive, and the pores are fully encapsulated. This allows three-dimensional (3D) analysis and evaluation of pore segmentation capability, which will be demonstrated in this study. High temperature direct bonding has previously been demonstrated [8, 9], which requires annealing temperatures above 1000 °C. In our study, we implemented a low temperature (≈ 400 °C) direct bonding [10, 11]. The chips (9.875 mm × 9.875 mm × 0.4 mm) were cleaned with solvent to remove residual photoresist. The chip surface was then cleaned with Piranha solution (volumetric mixture of 3 parts H_2SO_4 and 1 part 30 % (mass fraction) H_2O_2 in H_2O) followed by RCA1 (mixture of 5 parts H_2O, 1 part 27 % NH_4OH, and 1 part 30 % H_2O_2) to achieve hydrophilic surfaces. The chip surfaces were activated with O_2 plasma. The chips were stacked for initial bonding using a custom alignment tool and annealed at 400 °C for 1 hour in a N_2 atmosphere. Figure 6a shows one of the photomask designs with rectangular pores with rough surfaces mimicking those found in AM lack-of-fusion pores. The width of the cuboidal pores was fixed at approximately 200 µm, and the lengths varied from 400 µm to 4.42 µm in a geometric sequence with a ratio of $1/\sqrt{2}$. Half circles with diameter of 40 µm were super positioned around the perimeter to achieve rough surfaces. Figure 6b shows the corresponding SEM images of the holes created on a Si chip. The SEM image shows that all designed features were created. Figure 6c shows the corresponding XCT slice image of the bonded chip acquired at 6.30 µm/voxel resolution. X-ray source voltage of 80 kV and current of 56 µA with a 0.1 mm-thick Cu filter were used. A source-to-detector distance of 525.17 mm and a source-to-object distance of 22.06 mm were used. A flat panel detector with a pixel pitch of 150 µm was used. The projection images were acquired at 354 ms/projection for 4 frames/projection and 1000 projections. A standard Feldkamp-Kress-Davis (FDK) filtered backprojection reconstruction was carried out [12]. Most of the larger connected features are visible, but smaller disconnected features are not visible in the XCT images. The rough surface features are also not easily visible at the current resolution. Si provides similar contrast to those of aluminum alloys, and it is a potential surrogate material.

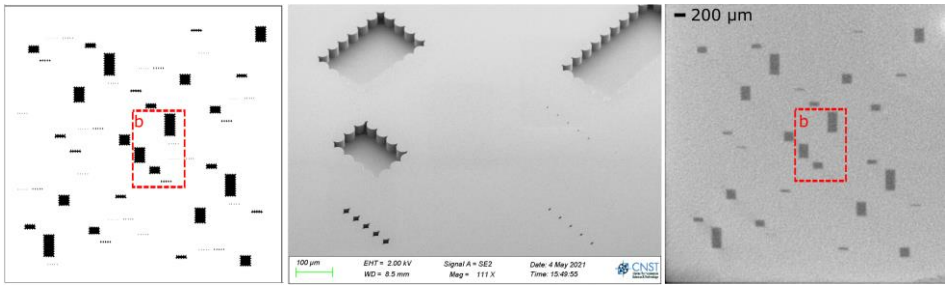

Figure 6: (a) Example photomask design, (b) SEM image of etched features, and (c) XCT image of bonded chips. The dashed boxes in a and c are the corresponding regions measured with SEM in b.

An image segmentation was carried out using the VGEasyPore algorithm (local contrast threshold: 10000, and local window size: 10 voxels). A median filter (3×3×3) was applied prior to the image segmentation. Figure 7a shows XCT images at horizontal and vertical cross sections. In the vertical cross sections (A-A and B-B at bottom of figure), it is not possible to observe any gap at the chip interfaces even with significant magnification of the images. Figure 7b shows the segmentation masks overlaid on top of the grayscale XCT images. The colormap is related to volume of the pores, and slight variation is observed for nominally identical pores. There are 16 nominally identical pores of each size in this phantom, and the segmented volume of the largest pore, for example, ranged from 0.002667 mm^3 to 0.001990 mm^3. The accuracy of segmentation results can be further evaluated based on the calibrated measurements acquired from SEM images.

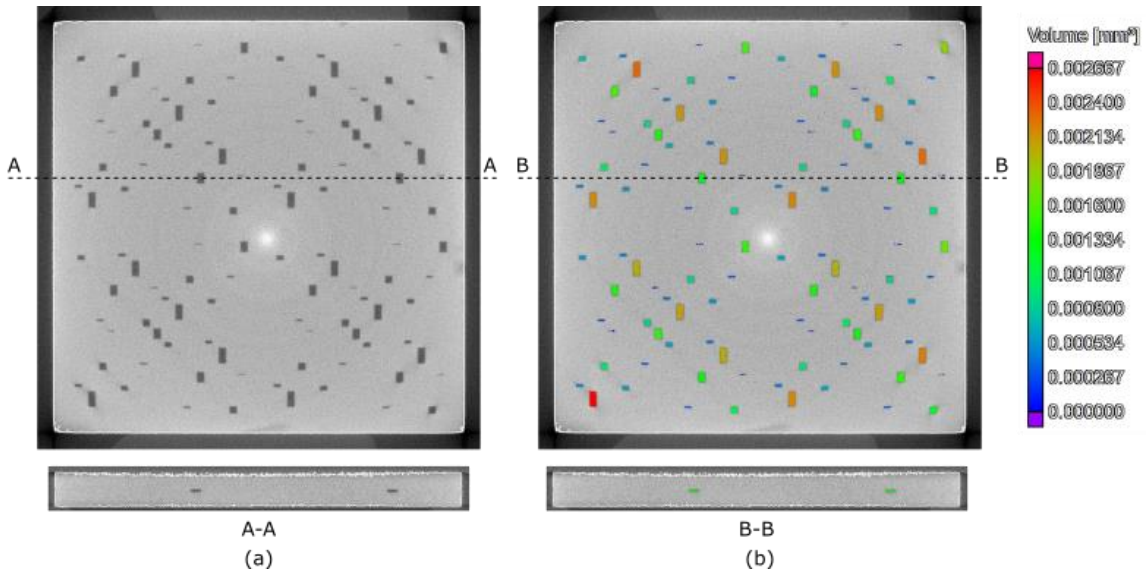

Figure 7: (a) XCT horizontal and vertical cross-sectional images of a bonded chip stack and (b) pore detection analysis carried out on XCT images.

5. CONCLUSIONS

We presented different approaches of generating controlled pores for inclusion in XCT phantoms. FIB was successful for generating blind holes of small sizes. Laser micromachining of blind holes for the chosen material and process parameters was not found to be promising. The concept of creating through holes in thin foils using laser micromachining, on the other hand, showed some promise. We plan to further investigate thin foil laser micromachining using an in-house laser marking system and associated assembly process to encapsulate the holes. Both FIB and laser micromachining can be implemented on most metallic materials of interest to the metal AM community. Stepper photolithography with DRIE allowed flexibility of generating complex pore structures accurately and repeatably. The method is promising for fabricating a phantom with high throughput. We also demonstrated an assembly method for Si material using low temperature direct bonding. We will further investigate methods to stack multiple chips and wafer-level bonding to improve process flow and yield after dicing. SEM-based calibration of feature size will be further investigated destructively and non-destructively.

ACKNOWLEDGEMENTS

We would like to thank Liya Yu of Center for Nanoscale Science and Technology at NIST for providing training on the chemical cleaning process and for the helpful discussion on Si direct bonding. We would like to thank Yiliang Bao of Physical Measurement Laboratory of NIST for the fruitful discussion and suggestions on Si direct bonding. We would like to thank Li-Anne Liew of Material Measurement Laboratory of NIST for fruitful discussion on lithography process.

We would like to thank Jared Tarr of Engineering Laboratory at NIST for the support with fabrication of the chip alignment tool.

REFERENCES

[1] Weiß, D., Shi, Q., and Kuhn, C., "Measuring the 3D resolution of a micro-focus X-ray CT setup." 345-53.
[2] Staude, A., and Goebbels, J., "Determining the spatial resolution in computed tomography-comparison of MTF and line-pair structures." 1-9.
[3] ASTM E1695-20, [Standard Test Method for Measurement of Computed Tomography (CT) System Performance] ASTM International, West Conshohocken, PA(2020).
[4] Kim, F. H., Pintar, A. L., Moylan, S. P., and Garboczi, E. J., "The Influence of X-Ray Computed Tomography Acquisition Parameters on Image Quality and Probability of Detection of Additive Manufacturing Defects," Journal of Manufacturing Science and Engineering, 141(11), (2019).
[5] Kim, F. H., Pintar, A., Obaton, A.-F., Fox, J., Tarr, J., and Donmez, A., "Merging experiments and computer simulations in X-ray Computed Tomography probability of detection analysis of additive manufacturing flaws," NDT & E International, 119, 102416 (2021).
[6] Madou, M. J., [Fundamentals of Microfabrication and Nanotechnology, Three-Volume Set] CRC Press, Boca Raton, FL(2012).
[7] Li, X., Dentinger, A., Brault, M., Ross, W. R., Osterlitz, M., Fu, L., Wu, M., Price, J. S., De Man, B., Bueno, C., and Fitzgerald, P., "Toward Comprehensive Industrial Computed Tomography Image Quality Assessment: I. Phantom Design," Journal of Nondestructive Evaluation, Diagnostics and Prognostics of Engineering Systems, 3(3), (2020).
[8] Thousand, J. D., and Smith, S. T., "A direct silicon bonded reference object for performance assessment of computed tomography systems," Precision Engineering, 58, 16-24 (2019).
[9] Thomson, S. R. D., Perron, J. K., Kimball, M. O., Mehta, S., and Gasparini, F. M., "Fabrication of uniform nanoscale cavities via silicon direct wafer bonding," J. Vis. Exp., 83, e51179 (2014).
[10] Reiche, M., and Gösele, U., [Direct Wafer Bonding], (2012).
[11] Liu, Z., and DeVoe, D. L., "Micromechanism fabrication using silicon fusion bonding," Robotics and Computer-Integrated Manufacturing, 17(1), 131-137 (2001).
[12] Feldkamp, L. A., Davis, L. C., and Kress, J. W., "Practical cone-beam algorithm," Journal of the Optical Society of America A, 1(6), 612-619 (1984).